Compact Optical Fiber Sensor Based on Silica Capillary Tube for Simultaneous High Temperature and Transverse Load Measurement

Jiewen Zheng, Bo Liu, Lilong Zhao, Rahat Hllah, Yaya Mao, Jianxin Ren, and Tutao Wang

***Abstract*—An optical fiber sensor is proposed and experimentally demonstrated for simultaneous measurement of high temperature and transverse load. The sensor is designed by splicing a silica capillary tube (SCT) to a single-mode fiber (SMF) and then heating the SCT to form an air bubble. SCT simultaneously functions as a Fabry Perot (F-P) microcavity and an anti-resonant reflection waveguide. These sensing mechanisms lead to high contrast sensitivity values of temperature and transverse load (1.89pm/°C,190.48pm/N and 24.93pm/°C, 16.68pm/N). Remarkably, the temperature sensitivity of this sensor is eleven times higher than that of the current fiber-tip micro-cavity (2.1 pm/°C). The sensor is also more advantageous in quantitative production and practical application due to its low cost, ease of fabrication, good mechanical strength, and convenient reflection probe.**

***Index Terms*—Anti-resonant reflection waveguide, F-P microcavity, dual-parameter sensor, transverse load sensor, temperature sensor.**

I. Introduction

DUE to its unique advantages such as high sensitivity, fast response, small size, easy manufacturing, and strong anti-electromagnetic interference ability, optical fiber sensors have been widely studied and applied to the measurement of temperature [1], refractive index [2], magnetic field [3], and transverse load [4] in recent years. In practice, especially in complex and changing environments, measuring the transverse load at high temperatures and eliminating temperature crosstalk is a pressing issue. Previously, the long-period fiber gratings (LPFG) [5] and superstructure fiber grating [6] had been used to simultaneously measure temperature and transverse load. However, if the temperature is higher than 200°C, most type-I FBGs used for temperature sensing will be erratic [7]. Although type-II or regenerated FBGs fabricated with a femtosecond laser or ion beam etching have been reported to work well at high temperatures, their manufacturing efficiency is low at high costs [8], [9]. Recently, the simple SMF-SCT-SMF structure has been studied in [10]–[12], and it has been confirmed that it can work stably in the environment up to 1000 °C. In addition, the high-temperature transverse load sensor based on high birefringence fiber and a mode interferometer based on microstructure fiber were proposed [13]–[15]. However, the fabrication and structure of these types of optical fiber sensors are both complex, limiting their large-scale production and application. Furthermore, these sensors have a characteristic size of at least a few millimeters, making them inconvenient for small areas and fixed-point measurements. As a result, the goal has always been to simplify the preparation process and create an optical fiber sensor with a simple structure, small volume, good stability, and low cost.

In this work, we propose a reflective optical fiber sensor with high sensitivity for simultaneously measuring high temperature and transverse load. Splicing SCT and SMF together creates the sensor, which is then discharged at the end of SCT to form an air bubble. SCT acts as F-P microcavity and anti-resonant reflection waveguide concurrently. The phenomenon of the anti-resonant reflection waveguide is the envelope of the F-P interference edge in the reflection spectrum. These sensing mechanisms lead to high contrast sensitivity values of temperature and transverse load (1.89pm/°C,190.48pm/N and 24.93pm/°C,16.68pm/N). Low cost, simple fabrication, solid structure, and a convenient reflection probe, among other features, make the sensor promising for practical application.

II. Fabrication and Principle

The proposed sensor's structure is illustrated in Fig. 1(a). A section of SCT with an outer diameter of 150μm and an inner diameter of 75μm was spliced with the lead-in SMF, and then discharged the end of the SCT to form air bubbles. To avoid the hollow core of SCT collapsing at the fusion joint, the discharge capacity of the fusion splicer (Fujikura 80s) was set to -25bit and the discharge time was 300ms during the splicing process. The fusion splicer's discharge capacity was 100bits and the discharge time was 5000ms during the air bubble melting process, and the distance between the discharge position and the end of the SCT was adjusted to obtain air bubbles with different wall thicknesses. The whole manufacturing process

Manuscript received October 11, 2021; revised November 15, 2021; accepted November 22, 2021. Date of publication November 24, 2021; date of current version December 8, 2021. This work was supported in part by the National Key Research and Development Program of China under Grants 2018YFB1800901 and 2018YFB1800905, in part by the National Natural Science Foundation of China under Grants 62075097, 62075038, 61975084, 61935005, 61835005, 61822507, 62005125, 61775098, 61875248, 61727817, U2001601, 62035018, 61720106015, and 61935011, and in part by the Open Fund of IPOC (BUPT), Jiangsu talent of innovation and entrepreneurship, Jiangsu team of innovation and entrepreneurship. *(Corresponding author: Bo Liu.)*

The authors are with the Institute of Optics and Electronics, Nanjing University of Information Science and Technology, Nanjing 210044, China (e-mail: 403346219@qq.com; bo@nuist.edu.cn; 001967@nuist.edu.cn; rahat@nuist.edu.cn; 002807@nuist.edu.cn; 003458@nuist.edu.cn; 1920765116@qq.com).

Digital Object Identifier 10.1109/JPHOT.2021.3130572

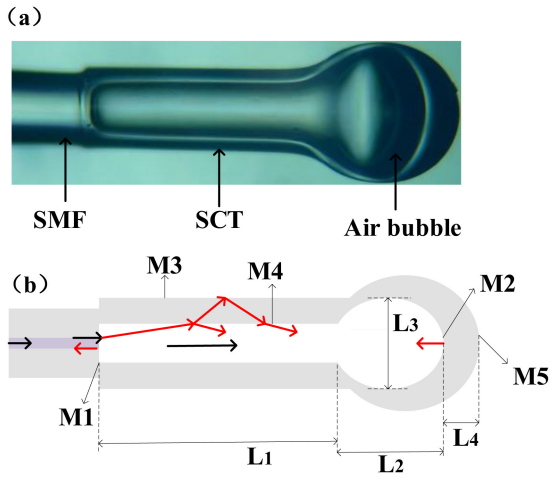

Fig. 1. (a) Schematic diagram of the proposed sensor. (b) The F-P interference and anti-resonant reflecting guidance mechanisms in the SCT.

includes only one splicing, so the sensor has good mechanical properties. The principle of the proposed sensor structure can be illustrated in Fig. 1(b). In the axial direction of the structure, the beam is reflected by M1 and M2 to form F-P interference, and the SCT acts as an F-P air. The interference dip of the $\mathrm{m}-th$ central wavelength can be expressed as [16]:

$$\lambda_{\mathrm{m}} = \frac{4L}{2\mathrm{m}+1} n_{\mathrm{air}} \tag{1}$$

Where $L = L_1 + L_2$ is the effective optical length of F-P interference and n_{air} is the refractive index of the hollow core.

The temperature sensitivity derived from F-P interference valley wavelength shift can be expressed as follows:

$$\frac{\partial \lambda_m}{\partial T} = \frac{4L}{2m+1} \cdot \frac{\partial n_{\mathrm{air}}}{\partial T} + \frac{4n_{\mathrm{air}}}{2\mathrm{m}+1} \cdot \frac{\partial L}{\partial T} = \lambda_{\mathrm{m}} \cdot \frac{\partial n_{air}}{n_{\mathrm{air}} \partial T} + \lambda_{\mathrm{m}} \cdot \frac{\partial L}{L \partial T} \tag{2}$$

Where $\partial n_{air}/n_{\mathrm{air}}\partial T$is the thermal optical coefficient (TOC) of air, and $\partial L/L\partial T$is the thermal expansion coefficient (TEC) of silicon material (5.5×10^{-7}/°C). From the latest Edlén, the refractive index of air is a function of pressure P(Pa) and temperature T(°C) [17]:

$$n_{air} = 1 + \frac{2.8793 \times 10^{-9} \times p}{1 + 0.003671 \times T} \tag{3}$$

In the ideal gas equation, $P/(T + 273.15)$ can be ρK approximate. $\rho$is the particle density of air, and K is the Boltzmann constant(1.381×10^{-23}J/K). Generally, it is 2.43×10^{25}/m^3 at 0.1Mpa, 25°C. The TOC of air can be calculated as -2.2×10^{-9}/°C. This value is negligible compared with the coefficient of thermal expansion of silicon materials.

When the light beam reaches the SCT sidewall in the radial direction, the beam reflected by the inner and outer walls M3 and M4 can also form F-P interference, and the SCT sidewall can be considered an F-P silicon cavity. The majority of light is lost through the sidewall at the central resonance wavelength, resulting in periodic transmission loss. More light is limited in the hollow core of SCT as the wavelength of light deviates from the central resonance wavelength, and light loss decreases. If the wavelength of the light is far from the resonant wavelength, the light is internally reflected and trapped in the hollow core of the SCT as a guide core mode. Therefore, the SCT also acts as an anti-resonant reflection waveguide. The $m'-th$ anti-resonance wavelength can be derived as [18]:

$$\lambda_{m'} = \frac{2d}{m'} \sqrt{n_1^2 - n_{\mathrm{air}}^2} \tag{4}$$

Where d and n_1 are the thickness and refractive index of the sidewall of the SCT, respectively.

The temperature sensitivity derived from wavelength shift of anti-resonant reflection waveguide can be expressed as follows:

$$\frac{\partial \lambda_{m'}}{\partial T} \approx \frac{2n_1 d}{m' \sqrt{n_1^2 - n_{\mathrm{air}}^2}} \cdot \frac{\partial n_1}{\partial T} = \lambda_{\mathrm{m}} \cdot \frac{n_1}{n_1^2 - n_{air}^2} \cdot \frac{\partial n_1}{\partial T} \tag{5}$$

Where $\partial n_1/\partial T$ is the TOC of silicon(1.1×10^{-5}/°C)

By comparing equations (2) and (5), the anti-resonant reflection waveguide is more sensitive to the temperature change than the F-P interference, because the TOC of silicon is much larger than its TEC. Therefore, the temperature sensitivity of the sensor is improved by introducing the anti-resonant cavity reflection waveguide mechanism. Here, setting n_{air}= 1.0, n_1= 1.445, and $\lambda_m = \lambda_{m'}$= 1550 nm, the temperature sensitivities based on the wavelength shift of the F-P interference valley and the anti-resonant wavelength are calculated to be 0.85 pm/°C and 22.6 pm/°C, respectively.

III. Experiment and Result Discussion

Three samples are made with different lengths(L) and thicknesses of the air bubble wall(d), named samples A, B, and C. Their microscope images are illustrated in Fig. 2(a). Because the field of view of the microscope is not enough to capture the whole sensor's image, Fig. 2(a) shows the splicing of two sensor images. The lengths of sample A, B and C are measured by microscope, L_1 are 386.4μm, 523.8μm, 827.3μm, L_2 are 245.5μm, 233.3μm, 293.1μm, the air bubble height L_3 are 250μm, 252.4μm, 279.3μm, the air bubble wall thickness L_4 are 63.6μm, 100μm, 75.9μm, respectively. The reflection spectrum of the samples is measured by a 3dB coupler with a broadband light source (BBS) of 1440nm∼1640nm and a spectrum analyzer (OSA, YOKOGAWA, AQ6370D) with a resolution of 0.5nm. The reflection spectrum of the three samples is illustrated in Fig. 2(b). As can be seen from Fig. 2(b), for each sample, the envelope of interference fringes is a periodic function of λ, which is caused by the anti-resonant reflection waveguide mechanism. The free spectrum range (FSR) of the anti-resonant reflection waveguide can be derived from equation (4) as:

$$FSR = \frac{\lambda_{m'} \lambda_{m'+1}}{2\mathrm{d} \sqrt{n_1^2 - n_{\mathrm{air}}^2}} \tag{6}$$

The wall thickness d of SCT of three samples is 37.5μm. Therefore, the FSR value calculated by equation (6) is 30.7nm, which is consistent with the measured value as illustrated in

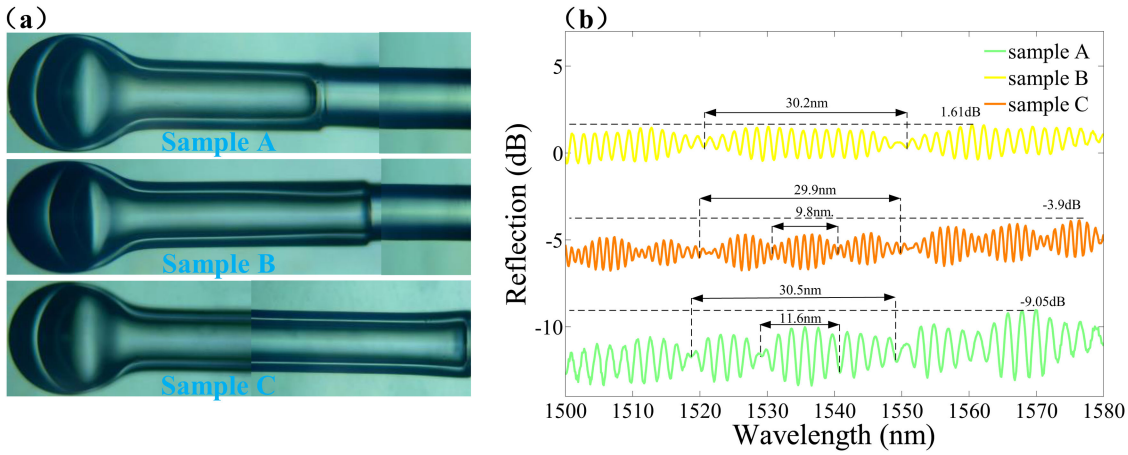

Fig. 2. (a) Optical microscopic images of the samples A, B and C. (b) The measured reflection spectrum of three samples at normal temperature.

Fig. 2(b). But we found that there is an envelope of other spatial frequencies of samples A and C with smaller air bubble wall thickness, but not in sample B with larger air bubble wall thickness. For the previous analysis, we simplify the influence of the reflector M5 on the F-P interference. Here we discuss the influence of the reflector M5 on the reflection spectrum. The total reflected intensity can be expressed as [19]:

$$\begin{aligned} I(\lambda) &= |E_1 + E_2 + E_3| \\ &= A_1^2 + A_2^2 + A_3^2 - 2A_1A_2\cos\left(\frac{4\pi n_{\text{air}}L}{\lambda}\right) \\ &\quad - 2A_2A_3\cos\left(\frac{4\pi n_1 L_4}{\lambda}\right) + 2A_3A_1 \\ &\quad \cos\left(\frac{4\pi(n_{\text{air}}L + n_1L_4)}{\lambda}\right) \end{aligned} \tag{7}$$

where E_1, E_2, and E_3 are the reflections of M1, M2, and M5; A_1, A_2, and A_3 are the amplitudes of E_1, E_2, and E_3, respectively; $L = L_1 + L_2$ is the cavity length, L_4 is the wall thickness, n_{air} and n_1 are the refractive index of hollow core and fused silica, and λ is the wavelength. Unlike two-beam interferences, E_3 can be either strengthen or weaken E_2, hence, modulating the entire spectrum with a slowly varying envelope, as discussed in the following. If the optical thickness of the wall, n_1L_4, satisfies:

$$\frac{4\pi n_1 L_4}{\lambda} = (2m+1)\,\pi \tag{8}$$

The phase difference between E_2 and E_3 will cause them to add in-phase and strengthen each other. Then equation (7) becomes:

$$I(\lambda) = A_1^2 + (A_2 + A_3)^2 - 2A_1(A_2 + A_3)\cos\left(\frac{4\pi n_{air}L}{\lambda}\right) \tag{9}$$

According to equation (8), the FSR can be calculated as:

$$FSR = \frac{\lambda^2}{2n_1L_4} \tag{10}$$

Samples A and C have FSR values of 12.8 and 10.5nm, respectively, as calculated by equation (10) and are consistent with the measured value shown in Fig. 2(b). When the air bubble wall thickness is large, the influence of M5 can be ignored, but when the air bubble wall thickness is small, the influence of M5 should be considered.

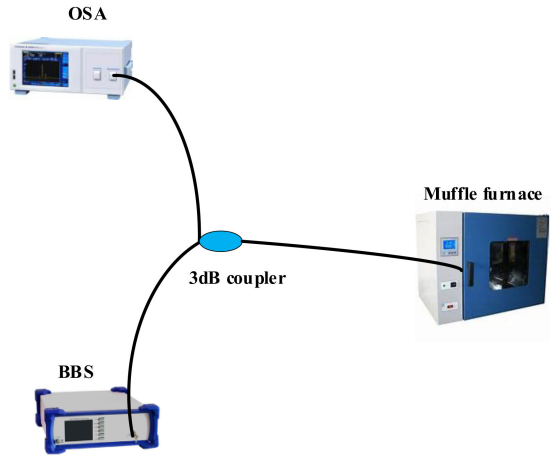

Fig. 3. Schematic diagram of the experimental setup for temperature response.

For a general anti-resonant reflection waveguide based on SCT, the resonance effect accumulates along the axial direction of SCT at the resonance wavelength. Therefore, in the optical fiber structure, the length of SCT will affect the visibility of the envelope. If the SCT is too short, the envelope cannot be observed. On the other side of the shield, the SCT should not be too long. With the increase in the length of the SCT, the visibility of F-P interference fringes decreases, which will also affect the performance of the sensor.

To study the temperature sensing performance of the sensor, as illustrated in Fig. 3, sample B was fixed in a muffle furnace with a built-in thermocouple, and the other end was connected to a 3dB coupler. BBS and OSA were used to monitor the incident light and the reflection spectrum, respectively. The temperature of the muffle furnace increased from 121°C to 541°C, and the interval is 70°C±1°C. At each temperature point, we recorded the reflection spectrum, as illustrated in Fig. 4(a) . It is obvious that with the increase of temperature, the envelope spectrum

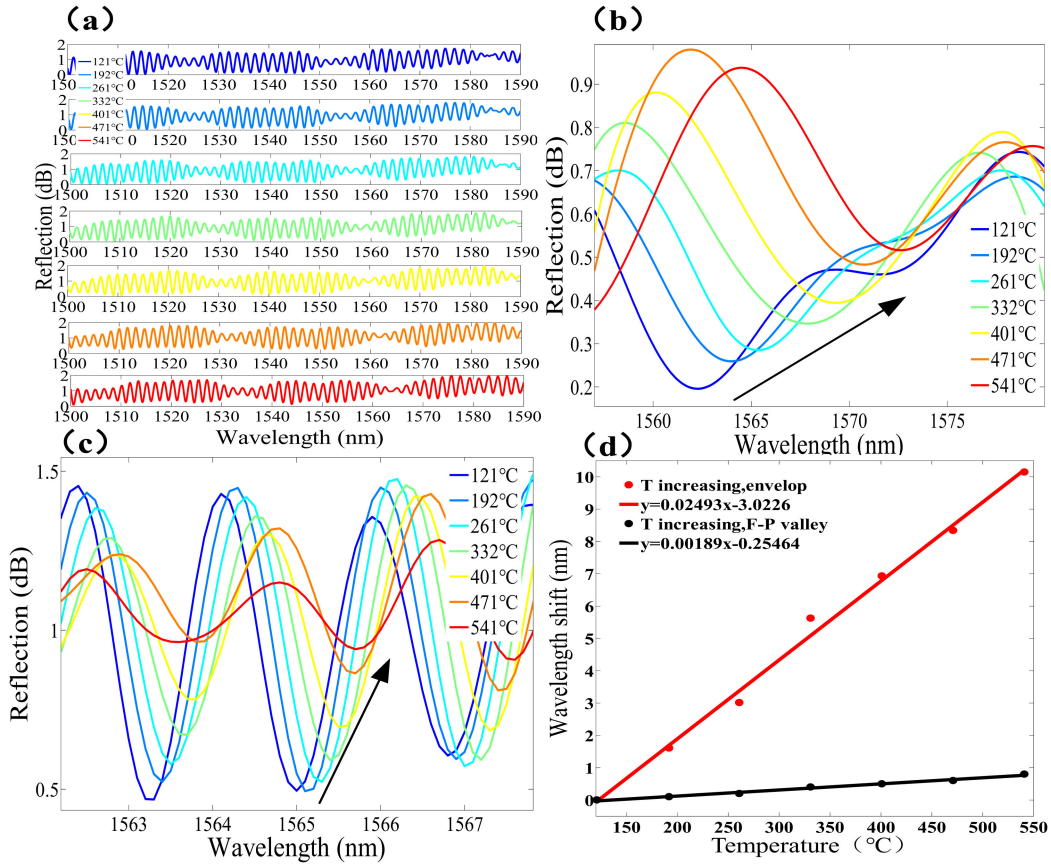

Fig. 4. (a) Reflection spectrum of sample B under different temperature. (b)-(c) The shift of the upper envelope and interference valley of the reflection spectrum around 1565 nm under different temperature. (d) The linearly fitting results of central wavelengths of the envelope and interference valley under different temperature.

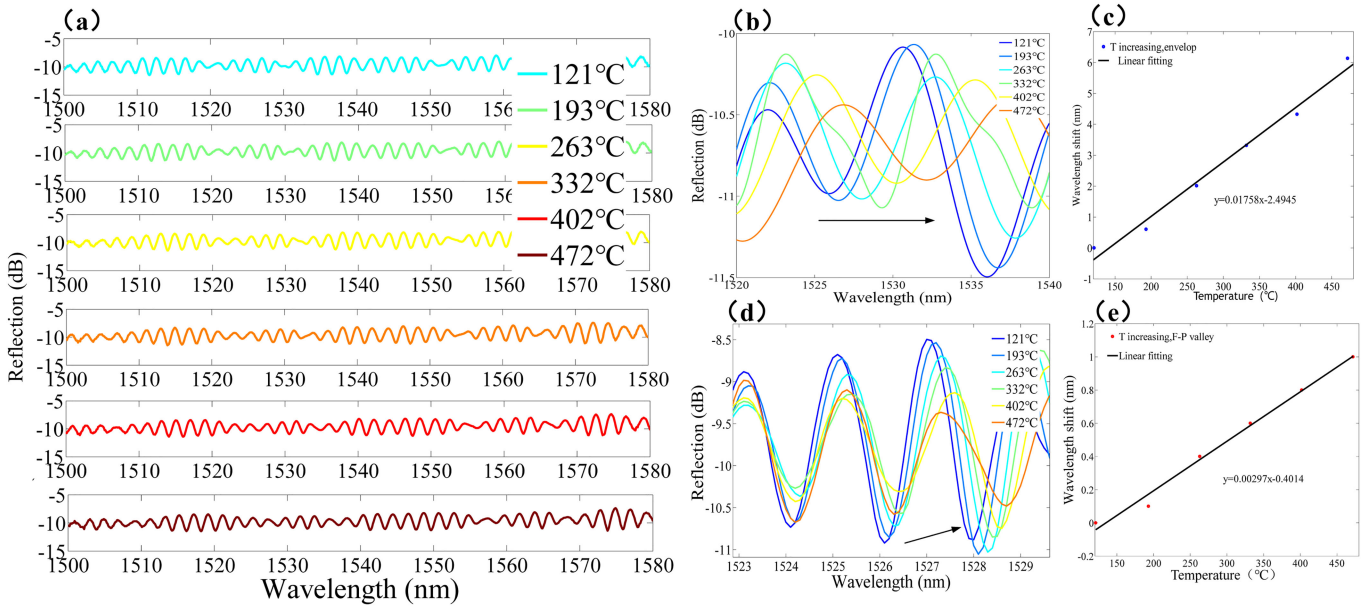

Fig. 5. (a) Reflection spectrum of sample A under different temperature. (b) and (d) The shift of the upper envelope and interference valley of the reflection spectrum around 1526 nm under different temperature. (c) and (e)The linearly fitting results of central wavelengths of the envelope and interference valley under different temperature.

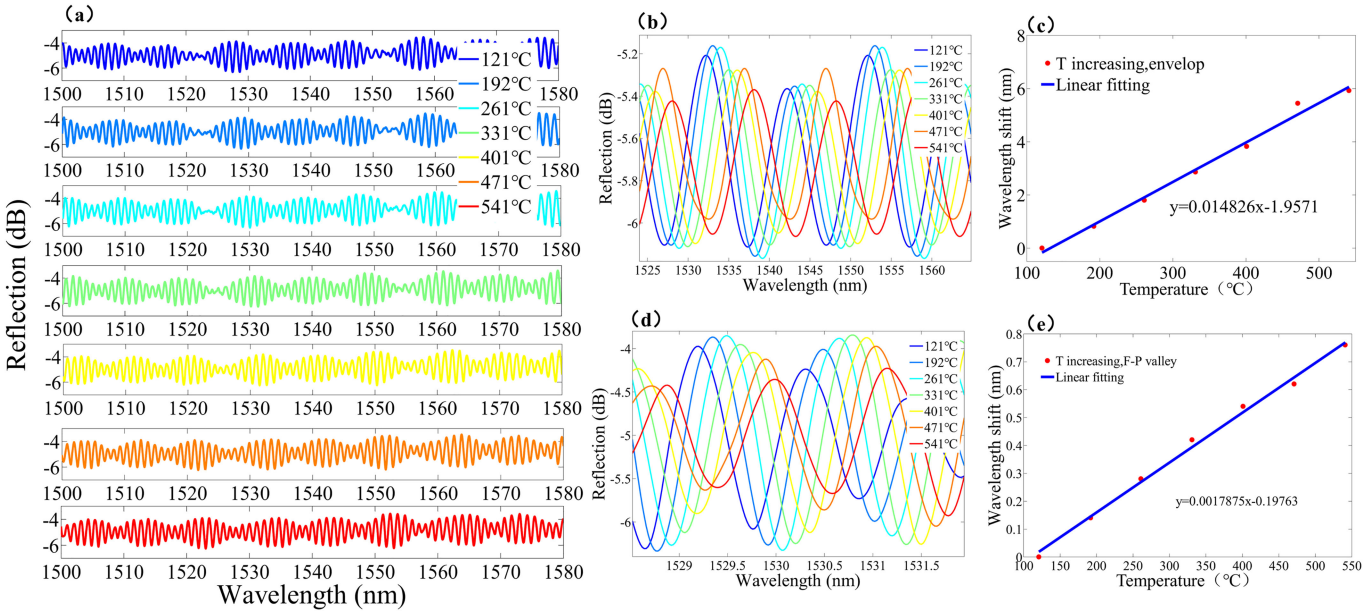

Fig. 6. (a) Reflection spectrum of sample C under different temperature. (b) and (d) The shift of the upper envelope and interference valley of the reflection spectrum around 1530 nm under different temperature. (c) and (e)The linearly fitting results of central wavelengths of the envelope and interference valley under different temperature.

moves to the direction of wavelength increase, while the F-P interference fringes almost have no wavelength shift.

The specific results of the lower envelope and the dip shift of the interference fringe near 1565nm were illustrated in Fig. 4(b) and (c), respectively. The linear fitting sensitivities of the envelope and F-P interference valley were 24.93pm/°C and 1.89pm/°C, respectively, as illustrated in Fig. 4(d). Due to the anti-resonant reflection waveguide mechanism, the temperature sensitivity of the sensor based on the wavelength shift of the envelope was much higher than that based on F-P, which had been verified in other sensing structures based on the anti-resonant reflection waveguide mechanism.

The response of samples A and C to temperature was tested using the same method in order to investigate the effect of wall thickness on temperature sensing performance. The reflection spectrum for sample A is shown in Fig. 5(a). Fig. 5(b) and (d) show the results of the lower envelope of sample A at 1528nm and the dip shift of F-P interference fringes, respectively. The envelope and F-P interference linear fitting temperature sensitivities of sample A at 1528nm were 17.58 pm/°C and 2.97 pm/°C, respectively, as illustrated in Fig. 5(c) and (e). For sample C, the reflection spectrum as illustrated in Fig. 6(a) The specific results of the lower envelope of sample C at 1530nm and the dip shift of F-P interference fringes were illustrated in Fig. 6(b) and (d). The linear fitting temperature sensitivities of the envelope and F-P interference valley at 1530nm were 14.83 pm/°C and 1.79 pm/°C, respectively, as illustrated in Fig. 6(c) and (e).

From the temperature experimental data of three samples, it can be seen that the three samples have similar low-temperature sensitivity based on F-P interference. For sample B, the sensitivity of the envelope is 24.93pm/°C, which is consistent with the calculated value in (5) is 22.6 pm/°C. For samples A and C,

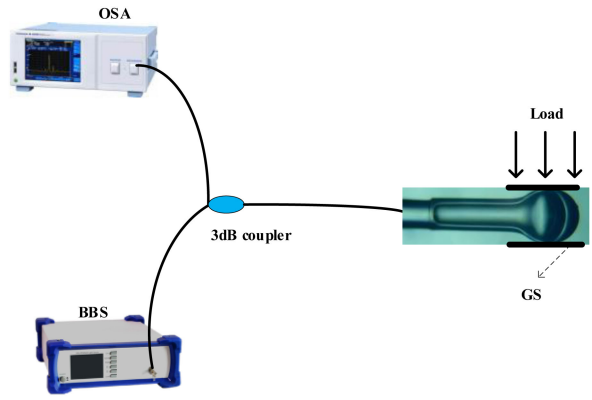

Fig. 7. Schematic diagram of the experimental setup for transverse load response.

the sensitivities of the envelope can be calculated to be by [14]:

$$\frac{\Delta\lambda}{\Delta T}=\left(\frac{L_4}{L_4\Delta T}+\frac{\Delta n_1}{n_1\Delta T}\right)\lambda=(\alpha+k)\,\lambda \qquad (11)$$

Where α is the TEC of the silica material, k is the TOC of the silica material. The sensitivities of the A and C envelope can be calculated to be 16.45 pm /°C, which is consistent with the measured value.

The transverse load sensing characteristics of sample B is also studied, which is placed horizontally between two parallel glass sheets (GS) to measure the transverse load, as illustrated in Fig. 7. As the transverse load increases from 0 to 3.5N, the reflection spectrum is illustrated in Fig. 8(a). The specific results of the lower envelope and the dip shift of the interference fringe near 1565nm were illustrated in Fig. 8(b) and (d),

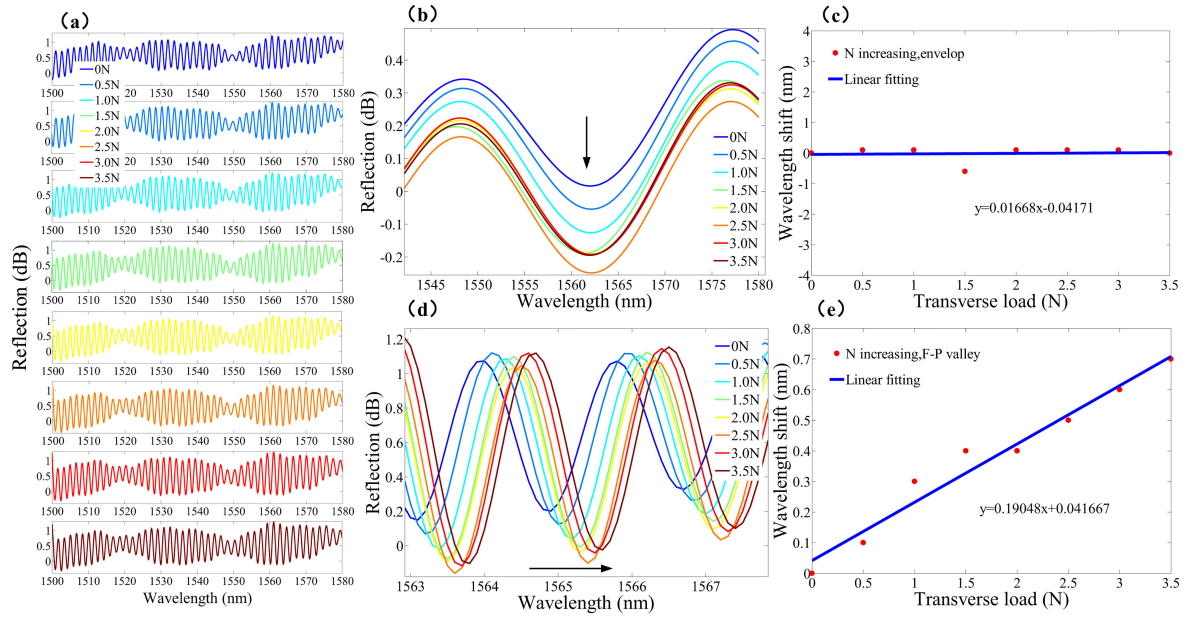

Fig. 8. (a) Reflection spectrum of sample B under different transverse load. (b) and (d) The shift of the upper envelope and interference valley of the reflection spectrum around 1565 nm under different transverse load. (c) and (e)The linearly fitting results of central wavelengths of the envelope and interference valley under different transverse load.

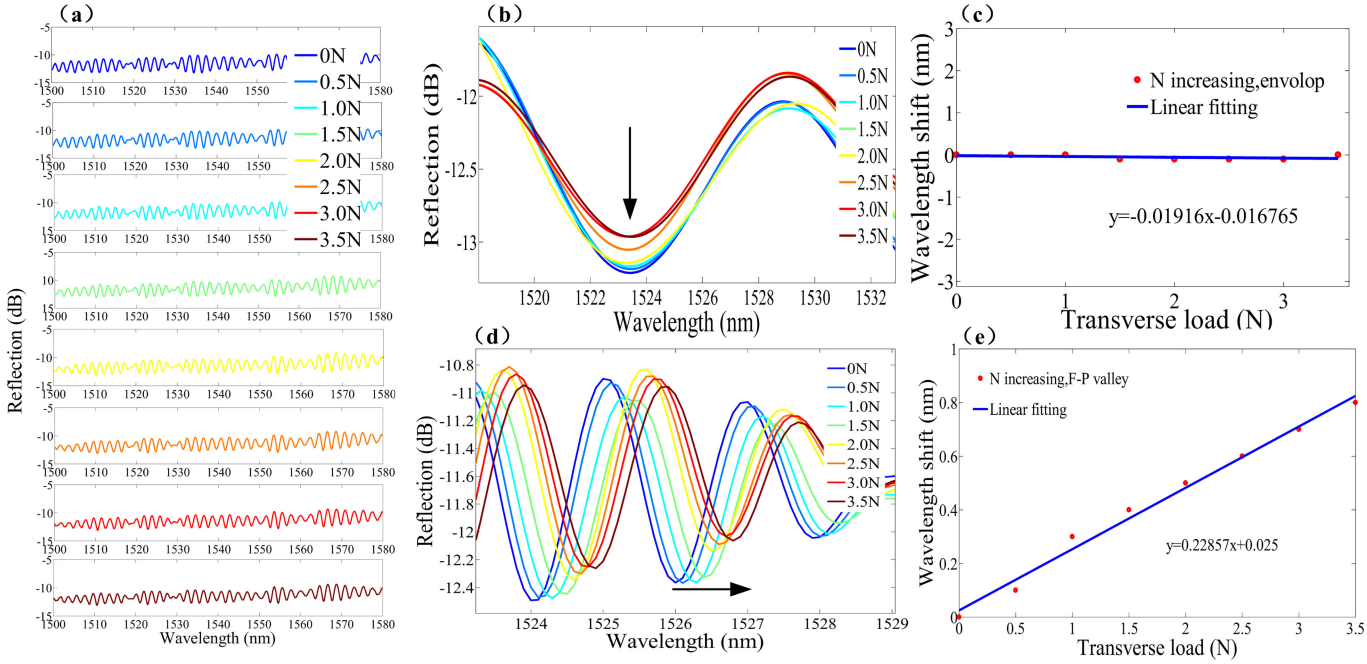

Fig. 9. (a) Reflection spectrum of sample A under different transverse load. (b) and (d) The shift of the upper envelope and interference valley of the reflection spectrum around 1526 nm under different transverse load. (c) and (e)The linearly fitting results of central wavelengths of the envelope and interference valley under different transverse load.

separately. The linear fitting sensitivities of the envelope and F-P interference valley were 16.68pm/N and 190.48pm/N, respectively, as illustrated in Fig. 8(c) and (e). Due to inaccurate recording of experimental data, the wavelength shift data of 1.5N in Fig. 8(b) and (d) were far away from the fitting curve. The envelope does not move basically, and the F-P interference valley shows a redshift, which may be due to the increase of the length of the air bubble under the action of transverse load, which almost does not affect the wall thickness of the SCT.

We also tested samples A and C for the transverse load. For sample A, the reflection spectrum is illustrated in Fig. 9(a). The specific results of the lower envelope and the dip shift of the F-P interference fringe of sample A near 1526nm were illustrated in

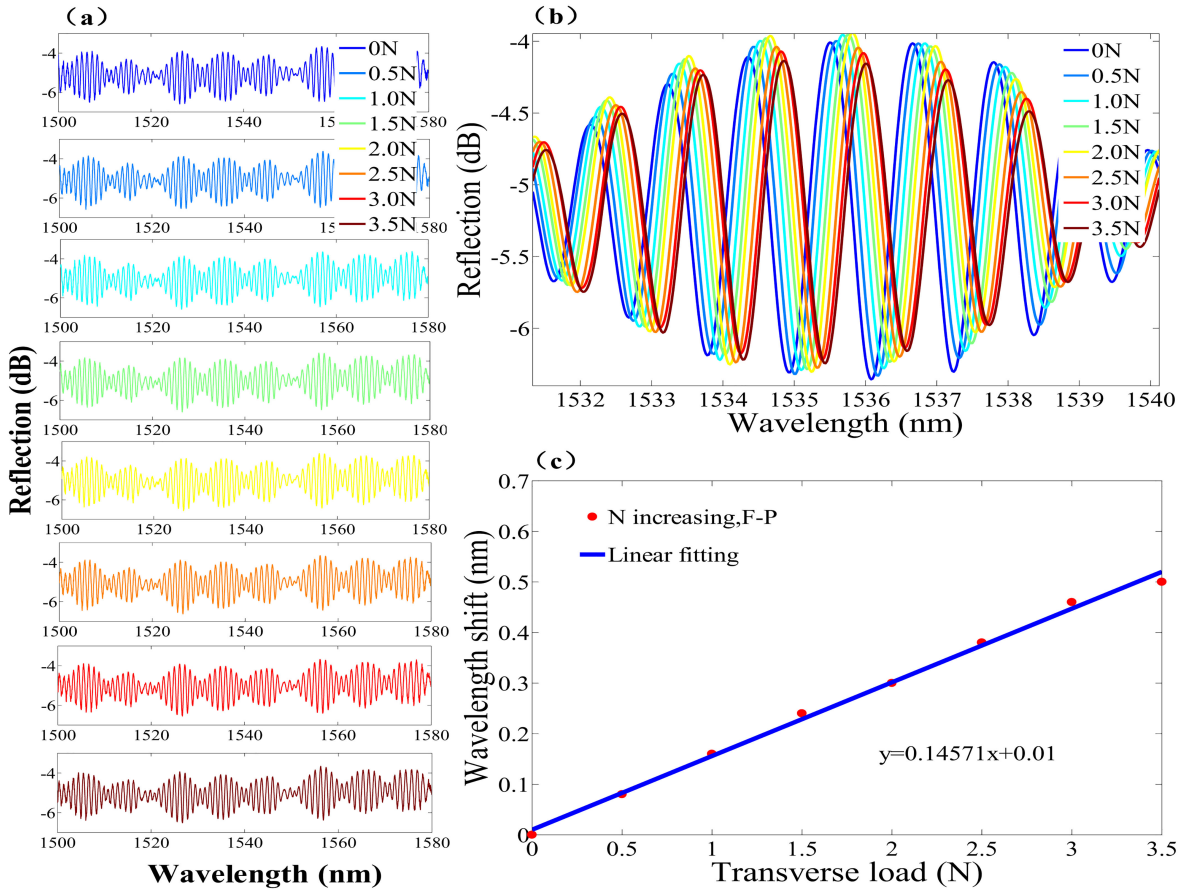

Fig. 10. (a) Reflection spectrum of sample C under different transverse load. (b)The shift of the interference valley of the reflection spectrum around 1535 nm under different transverse load. (c)The linearly fitting result of central wavelengths of the interference valley under different transverse load.

TABLE I
THE COMPARISON OF SENSORS FOR THE SIMULTANEOUS MEASUREMENT OF TRANSVERSE LOAD AND HIGH TEMPERATURE

Principle	High-temperature sensitivity	Transverse load sensitivity	Production difficulty	Probe type	Reference
FTMI	14.6pm/°C	-252.6pm/N	simple	Yes	[20]
Three-beam F-P	7.1 pm/°C	N	complex	Yes	[23]
Two-beam F-P	2.1pm/°C	1.37nm/N	simple	Yes	[14]
ARROW	18.19pm/°C	N	simple	No	[21]
HPCF	12.02pm/°C	4.45pm/(N/mm)	complex	No	[22]
SFG	40 pm/°C	57.73nm/(kg/m)	complex	No	[6]
Two-beam F-P+	20.3 pm/°C	1.53nm/N	complex	No	[24]
ARROW	24.93pm/°C	190.48pm/N	simple	Yes	This work

Fig. 9(b)and (d). The linear fitting sensitivities of the envelope and F-P interference valley were -19.16pm/N and 228.57pm/N, respectively, as illustrated in Fig. 9(c) and (e). It is confirmed again that the length of the air bubble increases under the action of transverse load, and the wall thickness of the SCT is hardly affected. For sample C, the reflection spectrum as illustrated in Fig. 10(a). The specific result of the wave dip shift of the F-P interference fringes of sample C at 1535nm as illustrated in Fig. 10(b). The linear fitting sensitivity of the F-P interference fringe was 145.71pm/N, as illustrated in Fig. 10(c).

In order to study the effects of different lengths $L = L_1+L_2$, air bubble height L_3, and air bubble wall thickness L_4 on the sensitivity of transverse load sensing, we define $K = L_3/L$, and k of samples A, B, and C are 0.395, 0.332, and 0.249, respectively. As illustrated in Figs. 8(e), 9(e), and 10(c), we found that the larger the K value, the higher the transverse load sensitivity of the sensor. In addition, the thickness of the air bubble wall does not affect the sensitivity of transverse load. Therefore, the transverse load sensitivity of the sensor can be improved by increasing K.

The comparison between this sensor and other reported sensors for simultaneous measurement of high temperature and transverse load is illustrated in Table I.

To extract the temperature and transverse load from the reflection spectrum, the central wavelength of the envelope and the

F-P interference valley must be monitored at the same time. One dip should be temperature-sensitive only, while the other should only be transverse load-sensitive. There are two temperature sensitivity values and two transverse load sensitivity values due to crosstalk sensitivity, and the matrix is required to demodulate the temperature and transverse load:

$$\begin{bmatrix} \Delta T \\ \Delta N \end{bmatrix} = \begin{bmatrix} s_{T1} & s_{N1} \\ s_{T2} & s_{N2} \end{bmatrix}^{-1} \begin{bmatrix} \Delta\lambda_1 \\ \Delta\lambda_2 \end{bmatrix} \tag{12}$$

Where $\Delta\lambda_1$ and $\Delta\lambda_2$ are the wavelength shift of F-P Valley and envelope valley, $\Delta T(^{\circ}C)$ and $\Delta N(N)$ are the change values of temperature and transverse load. s_{Ti} and s_{Ni} *(i = 12)* denote the temperature and transverse load sensitivities of a given dip, respectively.

The temperature sensitivity and transverse load sensitivity obtained by linear fitting in the experiment are substituted:

$$\begin{bmatrix} \Delta T \\ \Delta N \end{bmatrix} = \begin{bmatrix} 1.89 & 190.48 \\ 24.93 & 16.68 \end{bmatrix}^{-1} \begin{bmatrix} \Delta\lambda_1 \\ \Delta\lambda_2 \end{bmatrix} \tag{13}$$

Due to the anti-resonant reflecting guidance mechanism, the temperature sensitivity of the sensor when used for high-temperature detection alone is about twice that of [14]. At the same time, since the proposed sensor is based on pure fused silica, it can survive under the temperature even higher than 1000°C, which has been proved by other reported pure fused silica sensors[10]–[12]. Furthermore, it is not necessary to precisely control the length of SCT. The reflection spectrum of the sensor has obvious F-P interference fringes and an anti-resonance envelope dip when the initial cutting length of the SCT ranges from about 800μm to 1200μm. Although the length of SCT affects the sensor's transverse load sensitivity, the influence of inaccurate cutting can be eliminated by setting appropriate discharge parameters and discharge positions. Therefore, the common fiber cutting machine can be used to cut SCT, which makes quantitative production possible. In addition , the reflective probe makes the use of the sensor more convenient.

IV. Conclusion

A compact optical fiber sensor is proposed and experimentally demonstrated, which can simultaneously measure high temperature and transverse load by splicing a section of SCT to a SMF and discharging the end of the SCT to form an air bubble. By using the F-P microcavity and anti-resonant reflection waveguide, F-P microcavity has higher sensitivity to transverse load and the anti-resonance reflection waveguide has higher sensitivity to temperature. These sensing mechanisms lead to high contrast sensitivity values of temperature and transverse load (1.89pm/°C,190.48pm/N and 24.93pm/°C,16.68pm/N). Therefore, a matrix coefficient could be established for simultaneous measurement of high temperature and transverse load. In addition, it has the advantages of low cost, easy manufacture, solid structure, and convenient reflection probe.

References

[1] L. Xie, B. Sun, M. Chen, and Z. Zhang, "Sensitivity enhanced temperature sensor with serial tapered two-mode fibers based on the Vernier effect," *Opt. Exp.*, vol. 28, no. 22, 2020, Art. no. 32447.

[2] J. Li *et al.*, "Ultrasensitive refractive index sensor based on enhanced Vernier effect through cascaded fiber core-offset pairs," *Opt. Exp.*, vol. 28, no. 3, 2020, Art. no. 4145.

[3] Y. Zhao, R. Q. Lv, Y. Ying, and Q. Wang, " Hollow-core photonic crystal fiber Fabry–Perot sensor for magnetic field measurement based on magnetic fluid," *Opt. Laser Technol.*, vol. 44, no. 4, pp. 899–902, 2012.

[4] D. Chu *et al.*, "Temperature and transverse load sensing characteristics of twisted long period fiber gratings fabricated by femtosecond laser," *Opt. Laser Technol.*, vol. 96, pp. 153–157, 2017.

[5] Y. J. Rao, Y. P. Wang, Z. L. Ran, and T. Zhu, "Novel fiber-optic sensors based on long-period fiber gratings written by high-frequency CO_2 laser pulses," *J. Lightw. Technol.*, vol. 21, no. 5, pp. 1320–1327, May 2003.

[6] H. Chi, X.-M. Tao, D.-X. Yang, and K.-S. Chen, "Simultaneous measurement of axial strain, temperature, and transverse load by a superstructure fiber grating," *Opt. Lett.*, vol. 26, no. 24, 2001, Art. no. 1949.

[7] S. Wu, G. Yan, C. Wang, Z. Lian, X. Chen, and S. He, "FBG incorporated side-open Fabry-Perot cavity for simultaneous gas pressure and temperature measurements," *J. Lightw. Technol.*, vol. 34, no. 16, pp. 3761–3767, Aug. 2016.

[8] M. Ding, M. N. Zervas, and G. Brambilla, "A compact broadband microfiber Bragg grating," *Opt. Exp.*, vol. 19, no. 16, 2011, Art. no. 15621.

[9] C. R. Liao and D. N. Wang, "Review of femtosecond laser fabricated fiber Bragg gratings for high temperature sensing," *Photonic Sensors*, vol. 3, no. 2, pp. 97–101, 2013.

[10] S. Liu, J. Tian, S. Wang, Z. Wang, and P. Lu, "Anti-resonant reflecting guidance in silica tube for high temperature sensing," *IEEE Photon. Technol. Lett.*, vol. 29, no. 23, pp. 2135–2138, 2017.

[11] Z. Zhang *et al.*, "Hollow-core-fiber-based interferometer for high-temperature measurements," *IEEE Photon. J.*, vol. 9, no. 2, Apr. 2017, Art. no. 7101109.

[12] B. Feng, Y. Liu, and S. Qu, "High-temperature sensor based on resonant reflection in hollow core fiber," *Opt. Eng.*, vol. 55, no. 10, 2016, Art. no. 106127.

[13] T. Chen *et al.*, "Distributed high-temperature pressure sensing using air-hole microstructural fibers," *Opt. Lett.*, vol. 37, no. 6, 2012, Art. no. 1064.

[14] J. Ma, J. Ju, L. Jin, W. Jin, and D. Wang, "Fiber-tip micro-cavity for temperature and transverse load sensing," *Opt. Exp.*, vol. 19, no. 13, 2011, Art. no. 12418.

[15] C. Wu, H. Y. Fu, K. K. Qureshi, B.-O. Guan, and H. Y. Tam, "High-pressure and high-temperature characteristics of a Fabry–Perot interferometer based on photonic crystal fiber," *Opt. Lett.*, vol. 36, no. 3, pp. 412–414, 2011.

[16] C. R. Liao, T. Y. Hu, and D. N. Wang, "Optical fiber Fabry-Perot interferometer cavity fabricated by femtosecond laser micromachining and fusion splicing for refractive index sensing," *Opt. Exp.*, vol. 20, no. 20, 2012, Art. no. 22813.

[17] K. P. Birch and M. J. Downs, "An updated Edlén equation for the refractive index of air," *Metrologia*, vol. 30, no. 3, pp. 155–162, 1993.

[18] M. Hou*et al.*, "Antiresonant reflecting guidance mechanism in hollow-core fiber for gas pressure sensing." *Opt. Exp.*, vol. 24, no. 24, 2016, Art. no. 27890.

[19] Y. Zhu, K. L. Cooper, G. R. Pickrell, and A. Wang, "High-temperature fiber-tip pressure sensor," *J. Lightw. Technol.*, vol. 24, no. 2, pp. 861–869, Feb. 2006.

[20] C. Chen *et al.*, "Compact fiber tip modal interferometer for high-temperature and transverse load measurements," *Opt. Lett.*, vol. 38, no. 17, 2013, Art. no. 3202.

[21] N. Cai, L. Xia, and Y. Wu, "Multiplexing of anti-resonant reflecting optical waveguides for temperature sensing based on quartz capillary," *Opt. Exp.*, vol. 26, no. 25, 2018, Art. no. 33501.

[22] C. Fu *et al.*, " Transverse-load, strain, temperature, and torsion sensors based on a helical photonic crystal fiber," *Opt. Lett.*,vol. 44, no. 8, pp. 1984–1987, 2019.

[23] B. Xu, Y. M. Liu, D. N. Wang, and J. Q. Li, "Fiber Fabry-Pérot interferometer for measurement of gas pressure and temperature," *J. Lightw. Technol.*, vol. 34, no. 21, pp. 4920–4925, Nov. 2016.

[24] T. Nan *et al.*, "Three-parameter measurement optical fiber sensor based on a hybrid structure," *Appl. Opt.*, vol. 59, no. 27, 2020, Art. no. 8190.